Composites Science and Technology 279 (2026) 111585

Contents lists available at ScienceDirect

Composites Science and Technology

journal homepage: www.elsevier.com/locate/compscitech

Scalable structural supercapacitors with graphene-modified high-surface-area electrodes

Sian Ying Chen [a,1], Sourav Patranabish [a,1], Kathrin Weiland [a], Qixiang Jiang [b], Alexander Bismarck [b], Ludovic Jourdin [c], Kunal Masania [a,*]

[a] Shaping Matter Lab, Faculty of Aerospace Engineering, Delft University of Technology, Kluyverweg 1, 2629 HS, Delft, Netherlands
[b] Polymer and Composite Engineering (PaCE) Group, Institute of Materials Chemistry & Research, Faculty of Chemistry, University of Vienna, Vienna, 1090, Austria
[c] Department of Biotechnology, Delft University of Technology, Van der Maasweg 9, 2629, HZ Delft, Netherlands

ARTICLE INFO

Keywords:
Supercapacitor
Composites
Multifunctional
Fibre-fibre interface
Structural power composites

ABSTRACT

Electrification, including emerging technologies such as structural supercapacitors, is critical in realizing carbon-neutral transportation. A fundamental challenge is the trade-off between mechanical properties and energy storage capabilities. We report the fabrication of structural supercapacitors with a novel fibre-fibre interface to improve the interlaminar strength and encapsulation while considering the effect of structural resin on energy storage performance. The synthesized graphene nanoplatelets-modified electrodes attain a high specific surface area of ~231 $m^2\ g^{-1}$ - outperforming comparable carbon-based electrodes. We learned that the use of a gel-polymer electrolyte (GPE) separator containing 60 wt% Li-salt eliminates the requirement of electrolyte infusion and showed the highest values for conductivity for the cell produced using GPE. The implementation of glass fabrics (GFs) into the GPE improved the flexural modulus by ~22%, while retaining the mechanical strength of the cells. The multifunctional performance of the produced SSCs were on par or even outperformed the performances of SSCs reported in literature. A proof-of-concept prototype demonstrates that gel-polymer electrolyte cells can retain charges for longer than those with a glass fibre separator. Cumulatively, these offer the possibility of conventional composite manufacturing techniques to scale-up and eliminate delamination issues arising from different thermal expansion coefficients which also addresses the balance between mechanical stability and electrochemical performance. Our findings support the advancement of durable, lightweight energy storage and delivery systems for sustainable transportation, with potential applications in robotics and wearable technologies.

1. Introduction

Finding strategies to transition to a carbon-neutral society and reduce global carbon dioxide (CO_2) emissions is of critical importance. Reduction of CO_2 emissions from the transportation sector, which is a leading contributor, accounting for nearly one-fifth of global emissions, is necessary [1,2]. Therefore, electrification of the transportation infrastructure, including aviation and automotive sectors, is a top priority to facilitate advancements towards decarbonization [3]. However, the existing electrical energy storage technologies, e.g., lithium (Li)-ion batteries, face several fundamental drawbacks, such as low specific energy compared to traditional fuels, low specific power, longer charging times, and limited capability of delivering instantaneous power [4–6]. In uses such as aviation, the weight required per passenger for a given flight distance is nearly 24 times greater than that of kerosene [7,8]. Therefore, using only batteries to realize electric, emission-free mobility with improved range and power performance is unrealistic.

Structural energy storage devices, such as composite batteries [9,10] and supercapacitors [11–13], have recently emerged as promising candidates to overcome these limitations by combining mechanical load-bearing capabilities with energy storage functionality within a single material [14,15]. Structural energy storage devices are multifunctional fibre-reinforced polymer composites that can store electrical energy utilizing the mechanisms of either batteries or supercapacitors. Among these, structural supercapacitors (SSCs) are particularly important because of their unique capability to deliver instantaneous power

* Corresponding author.
E-mail address: k.masania@tudelft.nl (K. Masania).
[1] These authors contributed equally.

https://doi.org/10.1016/j.compscitech.2026.111585
Received 19 November 2025; Received in revised form 6 February 2026; Accepted 26 February 2026
Available online 27 February 2026

[11]. SSCs can be integrated with transportation systems' load-carrying components such as chassis, fuselage, and wings [16–18] offering a convenient, lightweight, and multifunctional alternative to conventional supercapacitors. However, for the realisation of SSCs, an optimal balance between the mechanical attributes and electrochemical efficiency is required [19]. Mechanical reinforcements, such as carbon fibres, may lower the capacitance and energy density by reducing the surface area available for charge storage [20,21]. Conversely, enhancing the electrochemical properties, e.g., using high-porosity or brittle electrode materials, can negatively affect the mechanical properties such as flexural strength and stiffness [22,23]. Additionally, environmental stability, cost-effectiveness, and compatibility are a few other factors to be considered for various adoption. Meeting these requirements is often challenging, and the lack of research on efficient encapsulation methods with high interlaminar strength and simple manufacturing methods for scale-up are the major bottlenecks in realizing SSCs for practical use cases.

To address these issues, researchers explored various strategies to enhance the electrochemical performance of SSCs while retaining their mechanical load-bearing capabilities [11–13]. Besides fabrication, the individual parts of an SSC, i.e. the electrodes, the separator, and the structural electrolyte, are also critical in achieving optimal multifunctionality. In particular, the fabrication process should retain the composite's stiffness, strength, and toughness while maximizing the proportion of electrochemically active regions. To this end, carbon fibres (CFs) have been identified as viable electrode materials for supercapacitors due to their favourable electrical conductivity and mechanical properties. However, their poor graphitization and low surface area (0.21 $m^2\ g^{-1}$) pose challenges to use in supercapacitors [24,25]. GNP coating has been introduced as viable surface modification of CF offering high BET surface area as well as excellent electrochemical properties. GNP provides an intact graphitic structure with high electronic conductivity, reduced defect density, and meso-scale inter--platelet spacing, enabling efficient ion access and stable electronic percolation [26]. Sanchez-Romate et al. [27] spray coated graphene nanoplatelets (GNPs) to increase the surface area of woven carbon fibres (WCF). However, using a surfactant while preparing the GNP solution, without adding a binder, resulted in poor attachment of GNPs to the fabric after matrix infusion. This caused a dragging effect, which led to the reaggregation of GNPs and the formation of GNP-rich areas. Other strategies to increase the SSA of CF include the integration of activated carbon or carbon nanotubes (CNT) [28] or reduced graphene oxide (rGO) [26]. However, these approaches suffer from various drawbacks, such as labour-intensive processes, inaccessible surface area, poor adhesion of the conductive species, and scalability issues.

SSCs require multifunctionality and demand that the carbon fibres and structural electrolytes possess electrochemical and mechanical properties. Solid electrolytes are formed by directly mixing salts in polymer matrices [29,30]. In contrast, dual-phase electrolytes consist of a solid phase that carries the mechanical load and a liquid or gel phase responsible for ion transport [11,31]. The dual-phase electrolyte matrix (containing Li-salts or ionic liquids) is often infused in fabric electrodes using vacuum-assisted resin transfer moulding [12,32]. In comparison, gel polymer electrolytes (GPE) consist of a polymer host swollen by a liquid electrolyte medium [33,34]. The GPE is reportedly produced as a film to serve as an electrolyte matrix and as the separator for both metal-fibre interface and fibrous interfaces [23,35]. GPEs have higher ionic conductivities over 1 mS cm^{-1} than solid polymer electrolytes (SPEs) from $10^{-5} - 10^{-2}$ mS cm^{-1} [11,36]. GPEs combine the diffusivity properties of liquid electrolytes with the chemical and mechanical stability of polymer chains. Nevertheless, GPEs are soft materials (ref PEO PVDF gel electrolytes); their mechanical properties should be improved to favour the application and processability of the SSC. Using GPEs that serve as both the electrolyte matrix and the separator in SSC yields higher energy storage performance [37]. Javaid et al. [36] compared different separator materials, e.g., filter paper, glass fabrics (GFs), and polypropylene (PP) membranes, for SSCs; filter paper showed the highest shear moduli and no delamination due to its good adhesion to the matrix. However, it had the lowest specific capacitance, possibly due to its pores being blocked by the structural resin part of the electrolyte matrix [11,30,36]. PP membranes had the highest specific capacitance because of its low thickness among the three materials. However, the PP separator had the lowest shear strength and modulus, which resulted in delamination and early mechanical failure due to poor adhesion. GFs had shear and electrical properties between the PP membrane and filter paper. Therefore, GFs are commonly selected as the separator material for SSCs [36,38]. Shirshova et al. [28] presented SSC prototypes using CF woven electrodes separated by woven GF with compression moduli up to 39 GPa and capacitances of up to 52 mF g^{-1}. Using a non-structural GPE matrix composed of polyacrylonitrile (PAN)/lithium bis(trifluoromethanesulfonyl)imide (LiTFSI) in conjunction with activated CF to produce supercapacitors led to an almost 20-fold increase in specific capacitance (55 mF g^{-1}) compared to that with as-received carbon fibres [39]. On changing from CF/PAN/LiTFSI to a multifunctional matrix (CF/PEGDGE/LiTFSI), the net effect was a decreased peak power density and energy density due to decreased ionic conductivity for both unmodified and activated CFs [28,39]. Although the mechanical properties were significant, the supercapacitor performance of these devices was not as envisaged.

Structural supercapacitors commonly rely on liquid electrolyte infusion, interleaved energy-storage layers, or nanocarbon coatings on carbon fibres – approaches that often weaken interlaminar interfaces and complicate composite manufacturing. In this work, a fibre–fibre interface–centric design is adopted, in which graphene nanoplatelet-modified carbon fibres function simultaneously as load-bearing reinforcements and electrochemically active electrodes, overcoming the limited surface area of conventional carbon fibres without disrupting structural continuity. The use of a gel polymer electrolyte (GPE) eliminates the need for electrolyte infusion and improves compatibility with established composite processing routes, while reinforcing fibres embedded within the electrolyte enhance mechanical robustness without degrading electrochemical performance. Collectively, this integrated design addresses key limitations identified in prior structural supercapacitors and advances multifunctional composites toward scalable and mechanically reliable energy-storage systems.

To evaluate this architecture, we fabricate SSCs comprising coated carbon fibre electrodes embedded in GPEs, which also function as a separator. We use a simple brushing technique to apply graphene nanoplatelets and binders aiming to increase the active surface area of CF-based electrodes. Two different types of cells are investigated – SSCs with a GPE separator, and SSCs with a GPE-impregnated GF separator. We anticipated that the utilization of GF separator will increase the mechanical properties of the GPE layer, which in turn will enhance the interlaminar strength of the SSCs. The SSCs were encapsulated into interleave composites; the electrochemical and mechanical performance were characterised. The content of Li-salt in the GPE material was varied systematically; the influence of GPE composition on the electrochemical performance was analysed.

2. Material & methods

2.1. Materials

High strength (HS) carbon fibre TeXtreme® spread tow fabric 1025 (0/90 plain weave, 200 g m^{-2}, epoxy compatible) was used as structural electrode fibres. Ethanol absolute (83813.360) was purchased from VWR International and graphene nanoplatelets (900407; CAS: 7782-42-5, <2 μm, m_w = 12.01 g mol^{-1}, grade C-750) were purchased from Sigma-Aldrich. Carbon conductive paint (05006-AB) was purchased from SPI Supplies. Poly (vinylidene fluoride-cohexafluoropropylene) (PVDF-HFP 427187), triethylphosphate (TEP 8.21141), bis(trifluoromethane)sulfonimide lithium (LiTFSI, 15224-50 GF), and sodium sulfate

decahydrate ($Na_2SO_4 \cdot 10H_2O$ - 403008) were purchased from Sigma Aldrich. Double-sided copper tape was purchased from 3M. Glass fibre fabric Hex Force® (E-glass, 0.15 mm thickness and 202 g m^{-2}) was purchased from Hexcel. EPIKOTE™ resin 04908 (epoxy) and EPIKURE™ 04908 curing agent were purchased from Suter Kunststoffe AG.

2.2. Electrode preparation

A plain weave carbon spread tow fabric (PW-CSTF) was subjected to heat treatment at 330 °C (determined by thermogravimetric analysis as explained below, results shown in ESI Fig. S1) for 30 min in a muffle

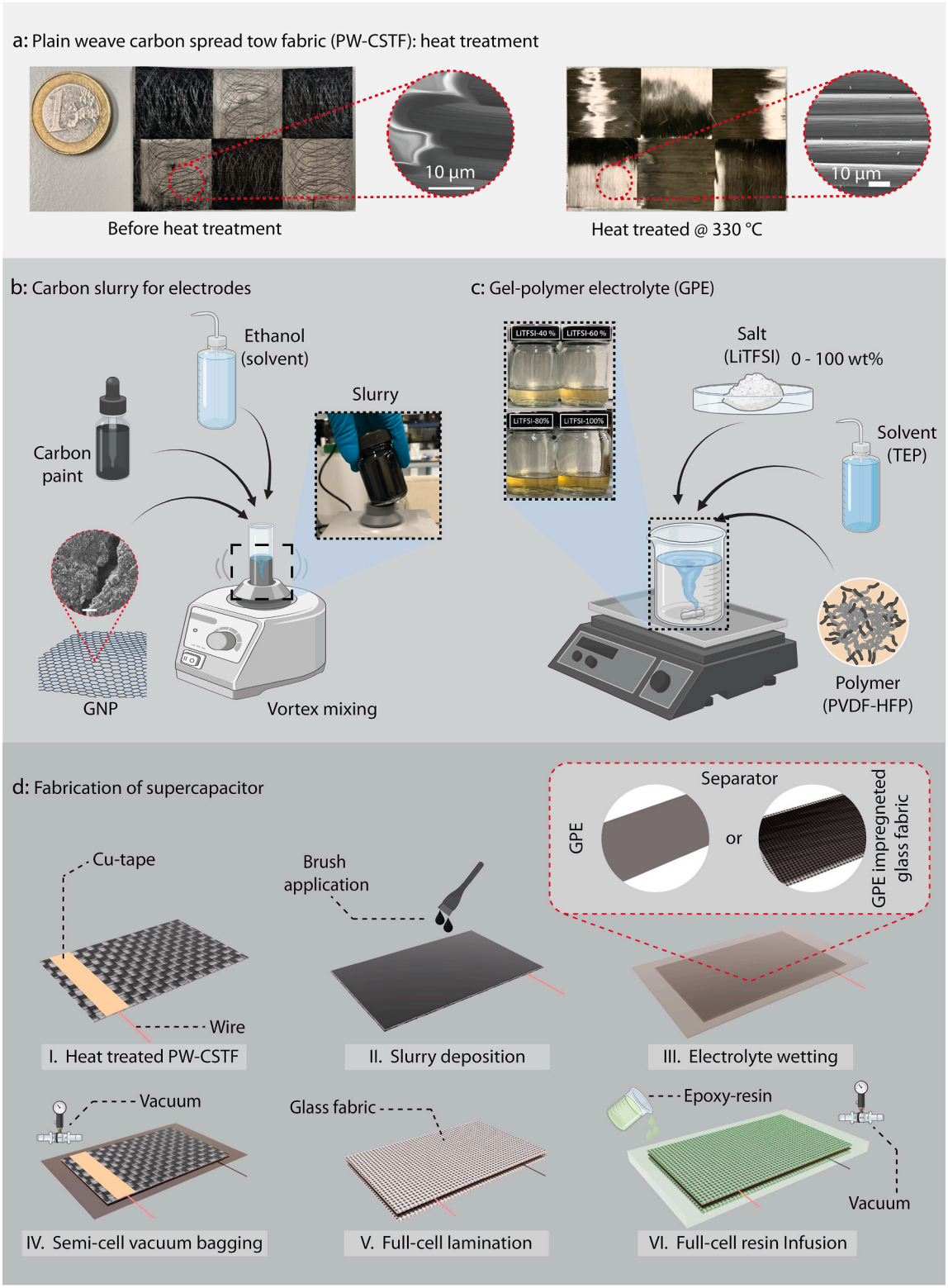

Fig. 1. Overview of fabrication process of SSC. a) Heat treatment on carbon fibre fabric. b) Preparation of carbon slurry for coating electrodes. c) Preparation of liquid gel-polymer electrolyte consisting of LiTFSI salt, TEP as solvent and PVDF-HFP as polymer. d) Fabrication and assembly route for the structural supercapacitors.

furnace (Nabertherm) in N_2 to remove sizing (Fig. 1a). A graphene nanoplatelet (GNP) slurry was produced by mixing 200 to 500 mg of graphene (GNP200 to GNP500) with 1 g of ethanol and 1 g of SPI carbon conductive paint as an adhesive between GNP and carbon fibres. This mixture was stirred for 1 h and then further homogenized using a vortex mixer (VV3, VWR) for 10 min (Fig. 1b). The resulting paint was then applied using a synthetic flat paintbrush (Qrea #12) onto a 20 mm × 40 mm or 60 mm × 40 mm surface area of PW-CSTF, whereby one or two brush strokes were applied (Fig. 1d). Subsequently, these coated electrodes were air-dried at room temperature in a fume hood until a stable sample weight was recorded.

2.3. Electrode characterisation

2.3.1. Thermogravimetric analysis of carbon spread tow fabric

To investigate a suitable temperature to remove binder and sizing from the carbon fibres, thermogravimetric analysis (TGA) was conducted using a PerkinElmer TGA 4000. The heating profile was determined with an initial temperature of 30 °C to a maximum temperature of 800 °C with a heating rate of 20 °C min^{-1} in N_2 (ESI Fig. S1).

2.3.2. Cyclic voltammetry measurements

Cyclic voltammetry was conducted to determine the areal capacitance of the coated CF electrode using a three-electrode setup in a standard glass electrochemical cell using a potentiostat (Metrohm Autolab). The working electrode consisted of the electrode specimen (20 mm × 40 mm) with copper tape attached to the end. An Ag/AgCl electrode was used as reference electrode, while a platinum mesh served as counter electrode. No stirring was applied during the measurements. Cyclic voltammetry was performed over a scanning range from 0 to 0.5 V across five cycles, with a specified scanning rate of 1 mV s^{-1} in a 1 M sodium sulfate solution. The total capacitance C_T was calculated using Equation (1):

$$C_T = \frac{\Delta Q}{\Delta V} = \frac{\int_0^{2V_0/v} i \vee dt}{2V_0} \quad (1)$$

where ΔQ is the total charge, ΔV the defined voltage range, and v the scan rate in the total voltage range (V_0) from 0 to 0.5 V. Subsequently the areal capacitance is calculated by normalising the total capacitance over the geometric electrode area.

2.3.3. Gas absorption analysis

The specific surface area of graphene nanoplatelets and produced electrodes was determined using the Brunauer-Emmett-Teller (BET) method from measured gas adsorption isotherms (NOVAtouch, Quantachrome Instruments). The electrodes were cut into small pieces and placed into glass sample cells. All samples were prepared by vacuum degassing. The slurry-coated plain weave carbon spread tow fabric (PW-CSTF) was subjected to a heating profile of 60 °C for 40 h, as the maximum service temperature for the SPI carbon conductive paint is 65 °C. Following degassing, the sample cells were fitted with 9 mm glass filler rods and immersed in a liquid nitrogen. The specific surface area was then determined by calculating the intercepts from the fitted linear curve using the volume of adsorbed gas at equilibrium (V), the monolayer gas quantity (V_m), the BET constant (K_{BET}), and the relative pressure (p/p_0).

2.3.4. Surface morphology

The surface morphology was examined using a JEOL scanning electron microscope (JSM-7500 F Scanning Electron Microscope) using an acceleration voltage of 5.0 kV.

2.4. Gel polymer electrolyte (GPE)

Polymer electrolytes with varying concentrations of LiTFSI, ranging from 40 wt% to 100 wt% relative to the amount of PVDF-HFP were produced. To prepare each solution, 9 g of TEP and 2 g of PVDF-HFP pellets were stirred at 550 rpm and heated to 70 °C for 4 h until fully dissolved. Once dissolved, LiTFSI in corresponding amounts was added to the polymer solution along with an additional 1 g of TEP. The glass vials were sealed with Parafilm, and the solution stirred at 65 °C and 250 rpm for 16 h (Fig. 1c). Finally, the polymer electrolyte solutions were degassed in a vacuum desiccator for 30 min. The liquid polymer electrolytes were subsequently cast using a film applicator (Sheen Instruments 1117/200 mm with speed control Erichsen (Model 509 MC-I)) onto glass plates (Riboglas Glashandel B.V.) with a gap of 800 μm to achieve uniform spreading. The gel polymer sheets were then vacuum-dried at 70 °C for 72 h. Fourier Transform Infrared (FTIR) spectroscopy (Spektrum 100, PerkinElmer) was conducted to characterise the functional groups present in both the wet and dried electrolytes, and compared to the raw materials. Scans from 500 to 3200 cm^{-1} were performed.

2.5. Structural super capacitor (SSC) cells

2.5.1. Cell assembly

For cell assembly, the electrode (60 mm × 40 mm) coated with a slurry containing 300 mg of graphene nanoplatelets (GNP300) and the GPE (40 wt% to 100 wt%) were assembled. A 12 mm copper tape was attached to the uncoated side of PW-CSTF electrodes and used as the current collecting terminals. A batch of cells were assembled by sandwiching GPE (65 mm × 45 mm) as the separator between two GNP300 coated PW-CSTF electrodes. Another batch of cells were produced using two GPE-impregnated glass fabrics (GF) (70 mm × 50 mm) as separators (Fig. 1d), which were sandwiched between two GNP300 coated PW-CSTF electrodes. The inner surfaces of the electrodes (with and without GFs) were coated with the same liquid gel electrolyte. These were then vacuum pressed at 850 mbar and 70 °C for 24 h. Finally, the full SSC cells were placed between two GF fabrics having dimensions of 80 mm × 70 mm. The layups were infused with epoxy resin and hardener by vacuum-assisted resin infusion at 850 mbar followed by curing of the epoxy resin at that pressure and at room temperature for 24 h.

2.5.2. Cell characterisation

2.5.2.1. Electrochemical performance. Cyclic voltammetry (CV) of the cells were conducted using a potentiostat (Metrohm Autolab) in a range from 0 V to 0.8 V with a scan rate of 2 mV s^{-1} to evaluate their electrical double-layer behaviour and to determine the voltage window to prevent overcharging. Electrochemical impedance spectroscopy (EIS) was performed using an applied frequency of 0.1 Hz to 1 MHz with an alternating potential of 10 mV.

2.5.2.2. Mechanical property assessment of structural supercapacitors. Three-point flexural tests were performed on the fully assembled cells. To comply with safety measures, the cells were sealed with polyethylene (PE) foils during the test. PE pouch bags were used for containing the material and volatiles of the cells resulting from the failure. The flexural stress σ and strain ε were determined using Equations (2) and (3) following ASTM D7264 standard. The specimen dimensions were length: 84 ± 4 mm, width 68 ± 2 mm, and thickness: 2.1 ± 0.2 mm. The tests were conducted at a speed of 1 mm min^{-1}, using a support span of 57 mm (span-to-thickness ratio 27.3 ± 1.3), and up to a deformation of 7 mm.

$$\sigma = \frac{3PL}{2bh^2} \quad (2)$$

$$\varepsilon = \frac{8\delta h}{L^2} \tag{3}$$

where P is the applied load, L the support span, b the specimen width, and h the specimen thickness. The flexural modulus of elasticity E_f^{chord} is determined using the chord modulus method in Equation (4) in the strain range from 0.001 to 0.003:

$$E_f^{chord} = \frac{\Delta\sigma}{\Delta\varepsilon} \tag{4}$$

2.5.2.3. Demo set up. A demonstrator using the fabricated SSC cells to power electrical components was assembled using a simple series circuit containing a red LED and a 1Ω resistor. The cells were charged with a 1.4 V power supply and their discharge characteristics were recorded using an oscilloscope (Picoscope 5442D). The details of the measurements are described in section 3.

3. Results and discussion

Plain weave carbon spread tow fabric (PW-CSTF) were heat treated to remove sizing on the fibre surface (shown by the micrograph of PW-CSTF before and after heat treatment, Fig. 1a) and binder on the weave surface (disappearing of the circular marks on the weave, Fig. 1a). A GNP-slurry containing various amount of GNP (i.e. 200 mg to 500 mg) was brush coated onto the desized PW-CSTF. The GNP loading on PW-CSTF was controlled to be in the range of 1.7 mg cm^{-2} to 8.1 mg cm^{-2} (ESI Table T1). SEM micrographs confirmed the uniform distribution of the coating on the PW-CSTF surface (Fig. 2a, which uses GNP300 as representative, the SEM images of other coated PW-CSTF are included in ESI Fig. S4), proving the suitability of brushing coating approach. Electrodes prepared with a slurry containing 300 mg of GNP possessed specific surface area of ~231 m^2 g^{-1}, which is in an upper range among the reported carbon electrodes from the literature shown (ESI Fig. S5) [12,25,40–46]. Ding et al. [47] presented CF electrodes coated with activated carbon reaching surface areas of up to ~163 m^2 g^{-1} showing significantly less surface area. Increasing the GNP content beyond this level led to surface cracking and inhomogeneity due to excessive particle loading (Fig. 2b). During cyclic voltammetry (CV) within a potential range of 0 V to 0.5 V (Fig. 2c) of the GNP coated PW-CSTF against a Pt counter electrode and a Ag/AgCl reference electrode, no redox reactions occurred on the electrodes within the investigated potential range, indicating effective charge propagation at the electrode/electrolyte interface [48]. The electrodes coated with 200 mg and 300 mg GNP showed an ideal rectangular-shaped CV curve reflecting capacitive behaviour. This signifies a rapid charge and discharge process, with minimal resistive losses and a purely electrostatic charge storage mechanism. In contrast, electrodes loaded with 400 mg and 500 mg of GNP exhibited distorted CV shapes with blunted and slanted profiles, probably caused by surface crack defects which might potentially lead to a lack of electrical contact between GNP and carbon fibre current collectors in the supercapacitor setup. Considering the brushing coating quality and GNP loading (and thus resultant areal or specific capacitance, Fig. 2d), the CF coated with GNP300 slurry applied using two brush strokes, with an electrode-specific capacitance of 4.61 F g^{-1} and an areal capacitance of 1164.3 F m^{-2} was selected for SSC assembly.

GPE was produced by casting a solution containing PVDF-HFP as polymer phase, various amounts of LiTFSI, and TEP as solvent followed by drying. The thickness of the GPE films increased from 138 μm to 255 μm with increasing LiTFSI concentrations from 40% to 100% with respect to PVDF-HFP (ESI Fig. S7). Fig. 2e shows the FTIR spectra of the GPE and the impact of drying. The absorption band at 2984 cm^{-1} (1) corresponds to the —CH stretching vibration in TEP. The P—O stretching vibrations, observed at 1019 cm^{-1} (5) and 1261 cm^{-1} (3) in the GPE, are significantly reduced after drying, indicating structural changes during the process. Additionally, the P═O stretching vibration at 1261 cm^{-1} (3) decreases post-drying, due to removal of TEP. A residual of TEP is likely chelated to Li^+ ions from LiTFSI [49]. The dissociation of LiTFSI into Li^+ and $TFSI^-$ is further supported by interactions with —CF_3 groups present in PVDF-HFP, evident from the reduction of the bands at 1400 cm^{-1} (2) and 1134 cm^{-1} (5) [50]. The dissociation of LiTFSI and the interaction between Li^+ ions and TEP suggests the solvation of the Li-ions. This enhances the mobility and is crucial for efficient charge transfer in supercapacitors. An additional modification due to the interaction of LiTFSI with PVDF-HFP was observed in the change of the bands representing the crystalline PVDF-regions at 612 cm^{-1}, 761 cm^{-1} and 796 cm^{-1}, which shifted to higher wavenumbers at 615 cm^{-1}, 764 cm^{-1}, and 802 cm^{-1}, respectively (Fig. 2f) [51]. The amorphous region exhibits a band at 873 cm^{-1} signified an increase in transmittance, indicating the LiTFSI reaction with the amorphous HFP region of the PVDF-HFP. The reduction of crystallinity in the gel is beneficial for various reasons when utilized in supercapacitors. A more amorphous structure allows for better ion transport, reducing the overall resistance and improving discharge efficiency [52,53].

SSC cells comprising GNP coated PW-CSTF (GNP300) electrodes and GPE as gel electrolyte were produced and encapsulated in the glass fibre reinforced epoxy composites. The Nyquist plots for the cells (Fig. 3a) were fitted to interpret the various physical processes occurring within and between the electrode–electrolyte system. Frequency spectra were divided into distinct regions, each associated with specific electrical elements (insert in Fig. 3a). The plot shows a depressed semicircle in the high-frequency region (left of the Nyquist plot) followed by a non-vertical steep line with varying slope at lower frequencies. The x-intercept of the depressed semicircle at the high-frequency end relates to the electrode and electrolyte resistance R_1 in the equivalent circuit (inset Fig. 3a) [54–59]. The depressed semicircle can be attributed to electric double layer (EDL) formation at the electrode-GPE interface [60] and modelled by a parallel RC circuit. The difference between the x-intercepts on the Z' axis in the RC circuit represents the value of the associated resistance [61,62]. The vertical radius of this semicircle reflects the porous nature of the electrodes. For depressed semicircles, the usual capacitor in the circuit is replaced by a constant phase element (*CPE*) [60,63]. In *CPE*, the phase angle is defined by $\left(\frac{-\pi}{2}\right) \times n$ $(0 \leq n \leq 1)$, as compared to $\frac{-\pi}{2}$ for usual capacitors. The associated resistance (R_2 in the equivalent circuit) can be related to the charge transfer resistance [61,62]. We present the sum of R_1 and R_2 as the bulk resistance R_{bulk} in Fig. 3b. The non-vertical lines in the low-frequency region are associated with the formation of a thin diffuse layer by the loosely bound salt ions, where the ion concentration decreases with increasing distance from the electrode [64,65]. These are represented by frequency-dependent Warburg impedances (W_o and W_s) in the equivalent circuit and correspond to the distributed charge storage mechanism at the high-surface-area electrodes. Summarizing the overall physical phenomena, at very high frequencies, the ions cannot respond to the external electric field and the only dominant process is electronic conduction. As the frequency decreases, the ions start slowly to respond and accumulate at the electrode-electrolyte interface, forming the EDL and giving rise to charge transfer processes (semicircle). At further lower frequencies, the ion diffusion process from diffuse layer to the porous electrode starts to dominate (Warburg-like non-vertical line). Finally, at very low frequencies, the ions penetrate into the porous electrode structure leading to nearly pure capacitive behaviour, rendering steeper linear tail of the Nyquist plots and indicating efficient charge storage. The EIS measurements and related equivalent circuit fitting were performed multiple times, and in both the forward (decreasing frequency) and the reverse (increasing frequency) cycles. The experimental Nyquist plot and corresponding fitted curves for the reverse cycle are presented in ESI Fig. S9a. The values of different components obtained after equivalent circuit fitting, along with the calculated conductivities, are presented in ESI Tables T2-T6. We have also analysed the Bode phase

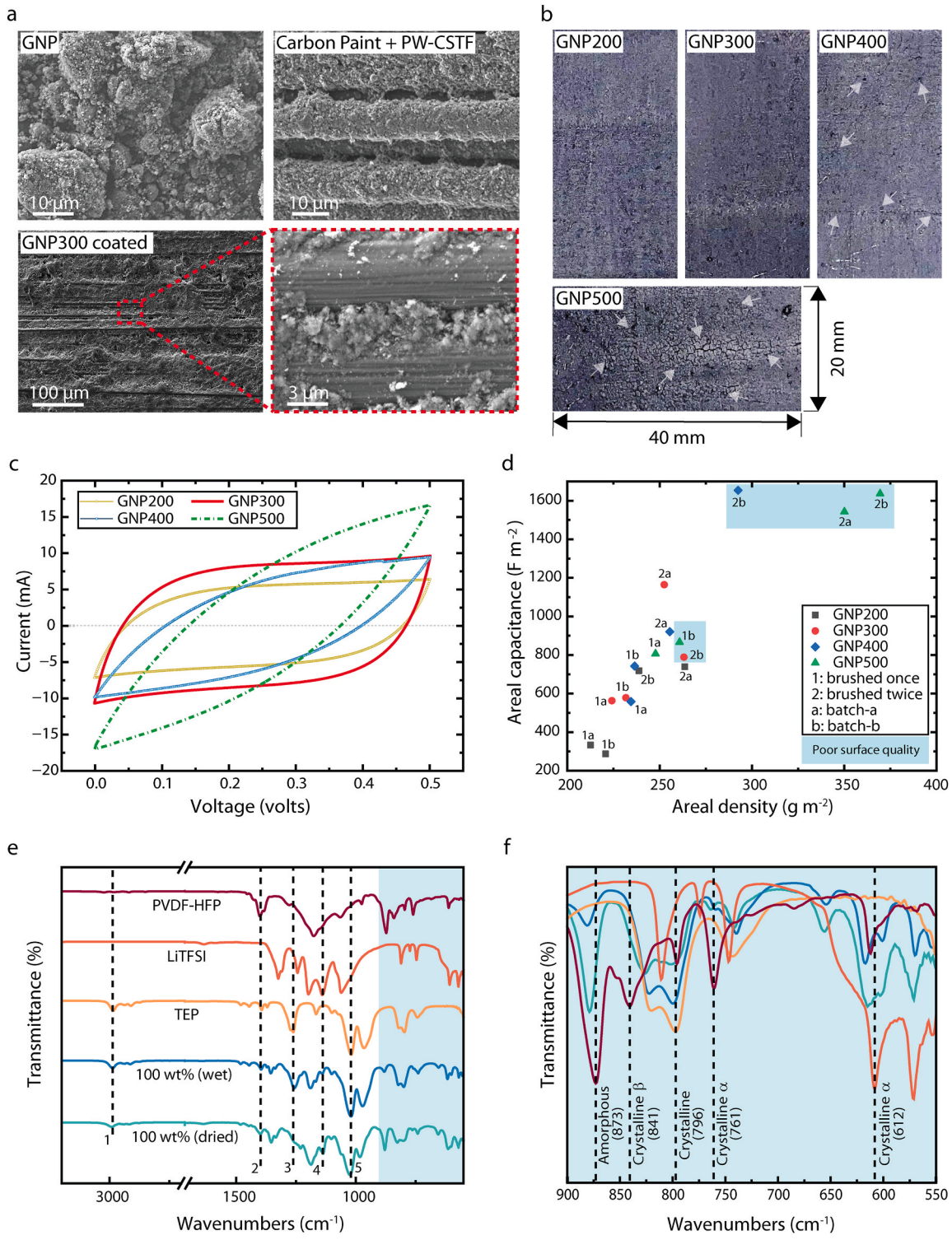

Fig. 2. Properties of the electrodes and the gel-polymer electrolyte. a) Scanning electron micrographs of utilized graphene nanoplatelets (GNPs), carbon paint-coated PW-CSTF carbon fibre electrode, and brush-coated electrode with slurry containing 300 mg GNP. b) Produced electrodes with varying GNP content (200-500 mg) revealed a cracked morphology of the electrode surfaces when high GNP content was used. The white arrows are used for visual guidance to the cracks. c) Cyclic voltammetry of the produced electrodes with GNP loadings from 200 mg to 500 mg in a range of 0.0 V to 0.5 V at a scan rate of 1 mV s^{-1}. d) Areal capacitance and areal density (based on the geometric area) of the produced electrode batches utilizing one or two brush strokes of GNP coating. e) Fourier transform infrared (FTIR) spectrum of the components PVDF-HFP, LiTFSI salt and TEP, as well as wet (before drying) and dried GPE containing 100 wt% of Li-salts in a range of wavenumber 4000 to 500 cm^{-1}. f) Inset of the FTIR spectrum in the range 900 to 550 cm^{-1} highlighting the relevant crystalline peaks of PVDF-HFP.

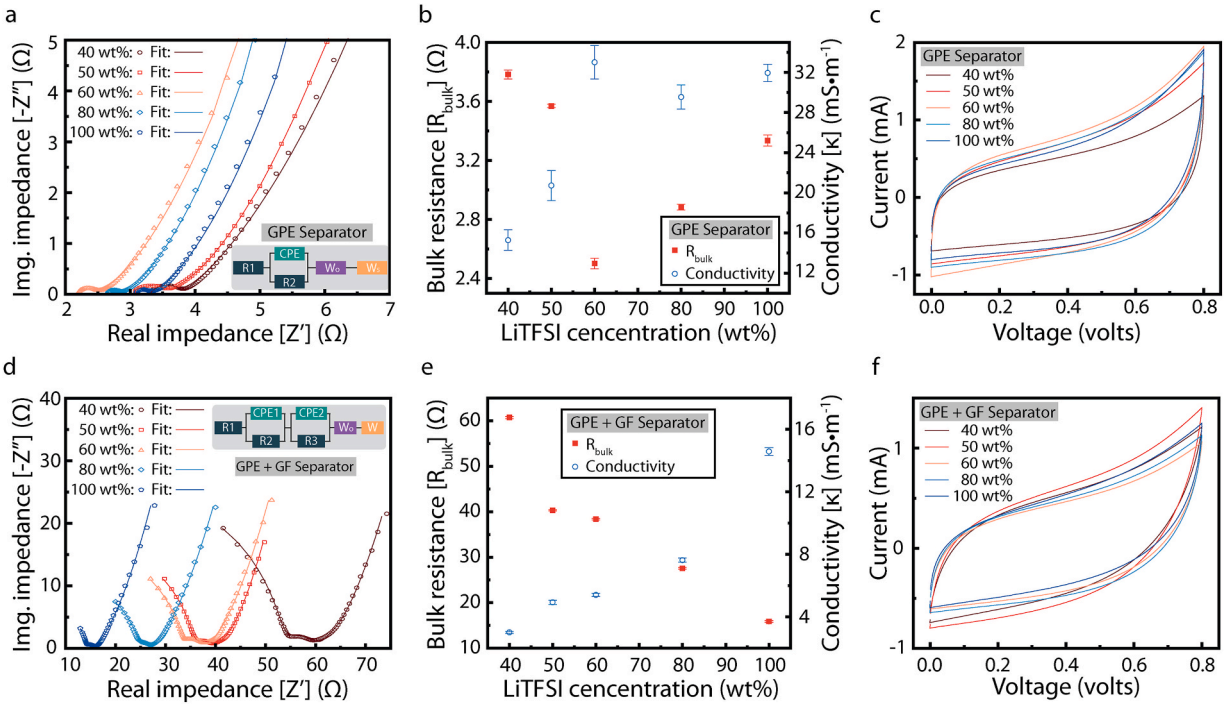

Fig. 3. Electrochemical properties of supercapacitor cells. Nyquist plots from the electrochemical impedance spectroscopy (EIS) measurements of the cells produced using a) GPE, and d) GPE + GF as the separator, respectively, with varying LiTFSI content (40 wt% to 100 wt%). The hollow symbols represent experimental data and the solid lines represent fitted curves, where the frequency increases from right to left. The insets show the equivalent circuits used to fit the data. Conductivity κ and bulk resistance R_{bulk} of b) GPE, and e) GPE + GF cells, as a function of LiTFSI concentration. Cyclic voltammetry curves of c) GPE, and f) GPE + GF cells in the potential window of 0.0 V to 0.8 V.

plots for all the cells to check consistency of the fittings. These are presented in ESI Figs. S8 and S10 for all the cells, and they show consistency and stability of the fitted equivalent circuit.

The calculated R_{bulk} and conductivity κ for all the GPE separated cells with varying concentrations of LiTFSI are presented in Fig. 3b. With increasing LiTFSI concentration from 40% to 60% in GPE, the number of free charge carriers (Li^+ ions) increased, resulting in decreasing R_{bulk} from 3.78 ± 0.03 Ω to 2.50 ± 0.03 Ω. Beyond 60 wt%, R_{bulk} starts to increase, lowering the effective conductivity possibly due to various effects, such as ion pairing (or association), clustering, increased viscosity, and phase separation (salt starts to crystallize) start to take place. A balance between ion transport pathways and structural integrity of the GPE was achieved at a Li salt concentration of 60% in GPE, which provided the electrode-electrolyte interface with well-distributed mobile ions, resulting in reduced bulk resistance and enhanced conductivity. Similar observations can be made from Fig. 3c, which shows the CV curves for all the GPE separated cells. The maximum current (1.95 mA) at the highest applied voltage and the highest specific capacitance (0.026 F g^{-1}) is achieved for the supercapacitor containing a GPE loaded with 60 wt% LiTFSI, which reduced thereafter with increasing Li-salt loading. The CV curves retained a quasi-rectangular shape for all the cells, indicating an ideal reversible behaviour. Until 0.5 V, no peaks associated with Faradaic reactions could be observed in the CV curves [27] suggesting the formation of an effective EDL capacitor. The CV curves become more distorted as the salt concentration increased.

The GPE + GF cells were produced aiming at reducing the risk of short circuit and to reinforce the GPE. The addition of GF resulted an increased thickness of GPE + GF films (430 μm to 550 μm, ESI Fig. S7). The Nyquist plots for the cells with GPE impregnated GF separators show an incomplete, depressed semicircle behaviour in the high-frequency region, followed by a small, depressed semicircle at intermediate frequencies, and a non-vertical steep line with varying slope in the low-frequency region (Fig. 3d). The additional depressed semi-circle (represented by CPE_2-R_3, insert in Fig. 3d) that appeared at higher frequencies must be due to the presence of GF in the SSC, which was determined by the smaller time constants ($\tau = RC$; where R is the resistance and C is the capacitance) compared to CPE_1-R_2, because the GF introduced high interfacial impedances to fast moving ions, and thus generating a high frequency response. The large vertical radius of this semicircle represents significant porous EDLC attributes introduced by GF, which also acted as barrier during charge transfer resulting in a higher associated resistance R_3. Consequently, the high-frequency x-intercept of the smaller semicircle, representing near the electrode-GPE interface (CPE_1-R_2), shifts to right side (low frequency) in the Nyquist plot. As the frequency decreases, the ions now need more time to reach and accumulate at the electrode surface. Consequently, they form an EDL at the electrode-GPE interface and give rise to charge transfer processes (smaller semicircle) with an expected larger charge transfer resistance (~2-8 Ω) compared to the GPE separated cells (0.2-0.5 Ω) (ESI Table T2-T5). The non-vertical lines following the depressed semicircuit related to frequency-dependent Warburg impedances (W_o and W), resulted from the formation of a diffuse layer near the electrode-GPE interfaces. SSC containing GPE + GF had 5 to 12 times higher R_{bulk} and low conductivity (Fig. 3e) compared to the corresponding SSC containing only GPE, indicating the dominating effect of GF hindering the charge transfer in GPE. In fact, the presence of GF screened the above-mentioned influence of high Li salt concentration on hindering ion transfer in GPE; as a result, in SSC containing GPE + GF, resistance of the cells simply decreased with increasing Li salt concentration.

The extracted parameter values from the equivalent circuit fitting, such as the resistances, CPEs, and goodness of fit (F_G), along with calculated conductivities are summarized in ESI Tables T2–T6. The reverse-cycle Nyquist plots and corresponding fitted curves are shown in ESI Fig. S9b, while the experimental and fitted Bode phase plots are presented in ESI Figs. S8 and S10. These plots and the excellent F_G values [$\sim O(10^{-5})$] demonstrate strong agreement between the model and the experimental data, validating the equivalent circuit for this system.

The CV curves for the GPE impregnated GF separated cells (Fig. 3f)

retain a quasi-rectangular shape and show no significant distortion or peaks associated with pseudocapacitive Faradaic reactions. It indicates an ideal reversible behaviour and capacitive charge storage mechanism, which is in line with the EIS observations. Compared to the GPE cells, the GPE + GF cells appear regular and rectangular in shape but with relatively smaller currents, which is due to the extra resistance introduced by GF. Another important observation is the lower enclosed area in these cells, as compared to the GPE cells suggesting that the GPE cells have higher capacitance compared to the GPE + GF ones, which completely agrees with the obtained specific capacitance values (ESI Fig. S13). Among all the GPE + GF cells, the highest capacitance is obtained for the cell with 50 wt% LiTFSI; in contrast to increasing ionic conductivity with increasing salt concentration (Fig. 3e). With further increased Li salt concentrations, the confined and porous geometry of the GFs may cause nonuniform wetting [66] and crowding or over-screening [67–69] of charges near the electrodes reducing the charge injection efficiency at the electrode interface and limiting the current [70]. Also, higher Li salt concentrations could lead to mass transport limitations, decreasing the overall current achieved during CV measurements. The observation also supports the specific capacitance peaking at 50 wt% for the GPE + GF cells and saturating at a lower value thereafter (ESI Fig. S13). These CV-based observations, together with the coulombic efficiency, discharge-specific energy and power, and long-term capacitance retention abilities (ESI Fig. S14–S16) indicate stable, durable and reversible electrochemical performance of the fabricated cells.

Representative flexural stress-strain curves for the SSC cells with GPE-separator and GPE + GF separator are shown in Fig. 4a and b, respectively. The flexural moduli of SSC containing GPE varied between 2.2 GPa and 3.5 GPa with varying LiTFSI concentration, resulting in an average flexural modulus of 3 GPa. The SSC with GPE had an average flexural strength of 60 MPa. The inclusion of two layers of GF did not affect the average flexural modulus and strength, which are 3.2 GPa and 57 MPa, respectively, indicating that the flexural properties of the SSC were dominated by the outer layer of GF/epoxy composite plies as well as the CF electrodes. For both types of SSC, the flexural moduli and strengths decreased with increasing SSC thickness (Fig. 4c) but increased with increasing cell density (ESI Fig. S18).

Both GPE and GPE + GF cell types demonstrated performance comparable to or exceeding that of existing SSCs reported in the literature [28,38,71,72]. Fig. 4e and f shows flexural chord moduli and the flexural strengths, respectively, as function of cell specific capacitance. Our SSCs demonstrated multifunctionality, i.e. data along the diagonal line of the plot, indicating a balance between flexural properties and capacitance. The cells produced using only a GPE separator performed slightly better than cells with introduced GF separator, signifying the greatest challenge of developing an SSC: the development of a multifunctional matrix/structural electrolyte, which simultaneously acts as electrolyte balancing ionic conductivity and structural properties allowing to hold the load-bearing fibre electrodes in place and transfer load. Xu et al. [38] employed two layers of unidirectional discontinuous fibre and GF separators of varying thicknesses to fabricate their SSCs. The results showed that thinner glass fibre separators achieved higher flexural stiffness than the thicker ones. This was attributed to a higher volume fraction of stiff carbon fibre electrodes, which improved the load transfer in flexure. Hudak et al. [71] used four layers of 120 gsm carbon fibre fabrics and two layers of 120 gsm GFs as separator. Despite their higher specific capacitance of 0.125 F g^{-1}, the mechanical properties were significantly lower than the flexural and chord modulus of our cells. Similarly, Senokos et al. [35] conducted flexural testing on SSCs with a metal-carbon fibre encapsulation. These samples were laminated using eight layers of 370 gsm carbon satin fabric, yielding high flexural modulus of 60 GPa and strength of 153 MPa. The specific capacitance, energy, and power density were 88 mF g^{-1}, 37.5 mWh kg^{-1}, and 30 W

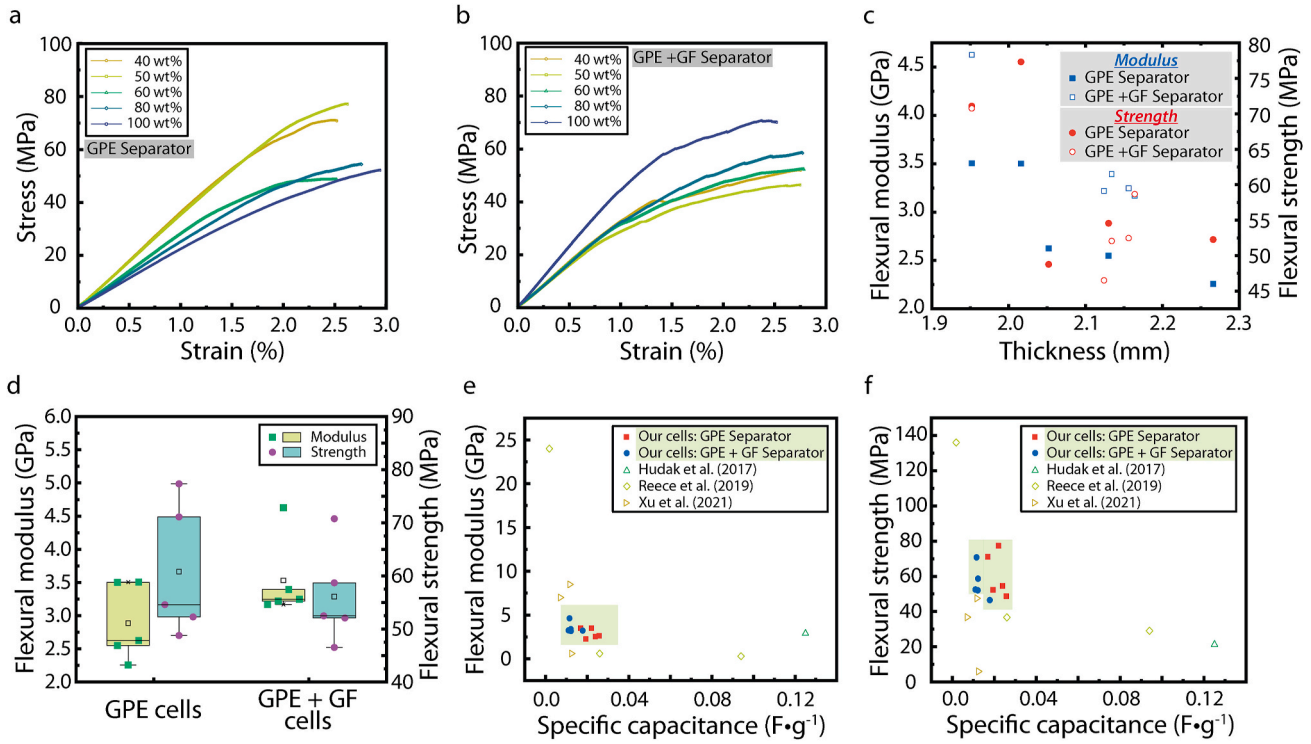

Fig. 4. Mechanical properties and multifunctionality of supercapacitor cells. Representative stress-strain curves from three-point bending tests of the cells produced using a) GPE separator, and b) GPE + GF separator. c) The flexural chord modulus and flexural strength of the cells as a function of the cell thickness. d) Box plots comparing the flexural chord modulus and flexural strength of GPE cells and GPE + GF cells. e-f) Comparison of multifunctionality (capacitive and mechanical properties) of the cells produced in this work with literature [38,71,72]: e) flexural chord modulus and f) flexural strength as a function of the cell specific capacitance. The data for the cells reported here are shown as hollow squares (purple) and circles (blue).

kg^{-1}, respectively. However, these values were normalized using only the SSC sample weight, rather than the full composite laminate. This on the other hand signifies the complicity in comparing produced SSCs with literature [15], as there is no reported standard testing or fabrication method. Qi et al. [73] reported a production route utilizing two GF for a multifunctional supercapacitor, achieving a capacitance of 0.49 F g^{-1} and an energy density of 150 mWh kg^{-1}, showing the importance of tailoring the separator weight fraction. A comparison of the structural layup, electrochemical and mechanical performance of the SSCs developed in this study with the literature is presented in Table 1.

To demonstrate the application of the fabricated cells in powering electronic components, we analysed the charge-discharge characteristic of the individual cells and connected a few of them in series to power a red LED. The red LED has a forward voltage of 1.8 to 2.0 V and a forward current of 20 mA. For this demonstration, first the GPE separated cells with 40, 50, 60, 80 and 100 wt% LiTFSI were chosen, referring to the observations made from EIS analysis in Fig. 3. Each cell was charged up to 0.7 V using a 1.4 V power supply through a 140 Ω resistor (charging circuit in Fig. 5a). To reach the desired voltage, all five of the GPE separated cells, along with the 100 wt% GPE + GF separated cell, were individually charged to 0.7 V and connected in series. A maximum voltage of 2.71 V was measured prior to discharge (ESI Video 1). The discharge was performed using the discharging circuit configuration (Fig. 5a) and the potential drop across the cells and the current through the series was monitored (Fig. 5b). The LED dimed out after 500 s, and the discharge energy was 0.08 J. Although the cells were able to power up the LED, it revealed a rapid self-discharge of the cells to reach a relatively steady state.

Supplementary video related to this article can be found at https://doi.org/10.1016/j.compscitech.2026.111585

To evaluate self-discharge behaviour, a self-discharge test was performed by charging individual cells to 0.7 V at a constant current of 10 mA, followed by setting the current to zero to simulate an open-circuit condition. The voltage response over time was recorded (Fig. 5c–d). For the cells produced using only GPE as the separator, the time required for the voltage to be halved increased (from 69 s to 173 s) with increasing salt concentration (Fig. 5c inset). In GPE-based SSCs, self-discharge is dominated by ionic redistribution rather than electrolyte leakage, as the quasi-solid nature of the PVDF-HFP-based gel suppresses macroscopic electrolyte flow. At higher salt concentrations, the increased availability of mobile charge carriers and stronger electric double-layer formation at the electrode-electrolyte interface enhance charge retention, thereby slowing the discharge process [74]. Similar salt-concentration-dependent self-discharge behaviour has been reported in polymer and hydrogel-electrolyte supercapacitors, where ion association and mobility govern charge relaxation dynamics [74]. Electronic leakage pathways through the composite are expected to be limited due to the insulating epoxy encapsulation and the physical separation of the electrodes by the GPE layer. However, localized electronic leakage at fibre-fibre interfaces or through imperfect electrode-electrolyte contact regions cannot be fully excluded and may contribute to the observed discharge rates, particularly in thin interlayers. In contrast, the cells produced with GPE-impregnated GF as separator showed consistent halving times of 80 s to 110 s (Fig. 5d inset), except for the 40 wt% cell (32 s) possibly due to lower ion concentration. The GF acts as a porous scaffold that redistributes the electrolyte and introduces tortuous transport pathways, reducing effective ion mobility. This created a generally slower effective ion transport resulting in a narrower range of discharge times which was relatively insensitive to the salt concentration [75]. While this stabilizes self-discharge behaviour, it also increases ionic resistance, consistent with the higher bulk resistance observed in EIS measurements (Fig. 3e). Based on these observations, the dominant self-discharge mechanisms in the reported system can be attributed to ionic redistribution and interfacial charge relaxation rather than electrolyte leakage. The potential mitigation strategies within the premises of the proposed SSC architecture could be to optimize the GPE composition balancing ion mobility and confinement, appropriate tailoring of the separator thickness and porosity, and improvements in the uniformity at the electrode-electrolyte interfaces. The total discharge time of each individual cell along with the corresponding half-time are presented in ESI Table T8.

4. Conclusions

We have successfully demonstrated the prototype production of multifunctional composites capable of simultaneously bearing mechanical load and storing and delivering electrical energy. Towards a scalable manufacturing approach, we adopted the brush-coating technique along with the incorporation of a binder and carbon conductive paint into the ink. It ensured a uniform and homogenous coating addressing challenges such as the delamination of graphene nanoplatelets from carbon fibres, which is detrimental for the electrochemical performance of the electrodes and thus of the structural supercapacitors. Moreover, the utilization of a gel polymer electrolyte as separator eliminated the need for electrolyte infusion, which is an important step towards streamlined fabrication. By systematically investigating the influence of Li-salt concentration on the electrochemical behaviour, it was highlighted that an optimal balance between ion transport pathways and structural integrity needs to be established. Although the introduction of a novel fibre–fibre interface via glass fabric

Table 1
Comparison of the structural constituents, electrochemical properties and mechanical performance of the reported SSCs with literature.

Sr No.	Electrode	Electrolyte	Specific Capacitance	Strength (MPa)	Modulus (GPa)	Energy density	Power density	Source
1	Carbon Aerogel/GNP coated CF	DGEBA-$LiClO_4$	0.354 F g^{-1}	8.7 (Shear)	2.6 (Shear)	0.8 Wh kg^{-1}	108 W kg^{-1}	Javaid et al. [41]
2	Activated CF	Epoxy:1 M + TEABF4/PC	0.1 F g^{-1}	29.1 (Flexural)	0.3 (Flexural)	5 mWh kg^{-1}	2 W kg^{-1}	Reece et al. [72]
3	CNT fibre interleaves/ FRP	Thermoplastic + $[PYR_{14}][TFSI]$	88 mF g^{-1}	153 (Flexural)	60 (Flexural)	37.5 mWh kg^{-1}	30 W kg^{-1}	Senokos et al. [35]
4	CNT grafted CF	MTM57+IL + LiTFSI	0.01 F g^{-1}	153 (Compression)	47 (Compression)	0.9 mWh kg^{-1}	0.021 W kg^{-1}	Greenhalgh et al. [76]
5	CF	PEGDGE + IL (EMITFSI)	10.7 mF g^{-1}	5.36	0.3	0.015 mWh kg^{-1}	0.003 W kg^{-1}	Qian et al. [77]
6	CAG-CF	PEGDGE + IL (EMITFSI)	71.2 mF g^{-1}	8.71	0.9	0.10 mWh kg^{-1}	0.004 W kg^{-1}	Qian et al. [77]
7	Polyaniline-ACF	DGEBA + $LiClO_4$	22.2 mF g^{-1}	6.3	1.0	49.4 mWh kg^{-1}	21.6 W kg^{-1}	Javaid et al. [78]
8	CF	PVDF + LiTf	11.62 mF g^{-1}	47.49 (Flexural)	8.48 (Flexural)	–	–	Xu et al. [38]
9	CF	PEG-LiTf	4.7 mF g^{-1}	16.74 (Flexural)	3.16 (Flexural)	17.4 mWh kg^{-1}	–	Hudak et al. [71]
10	GNP modified CF	PVDF-HFP + LiTFSI	25.72 mF g^{-1}	77.3 (Flexural)	4.62 (Flexural)	2.08 mWh kg^{-1}	0.026 W kg^{-1}	This work

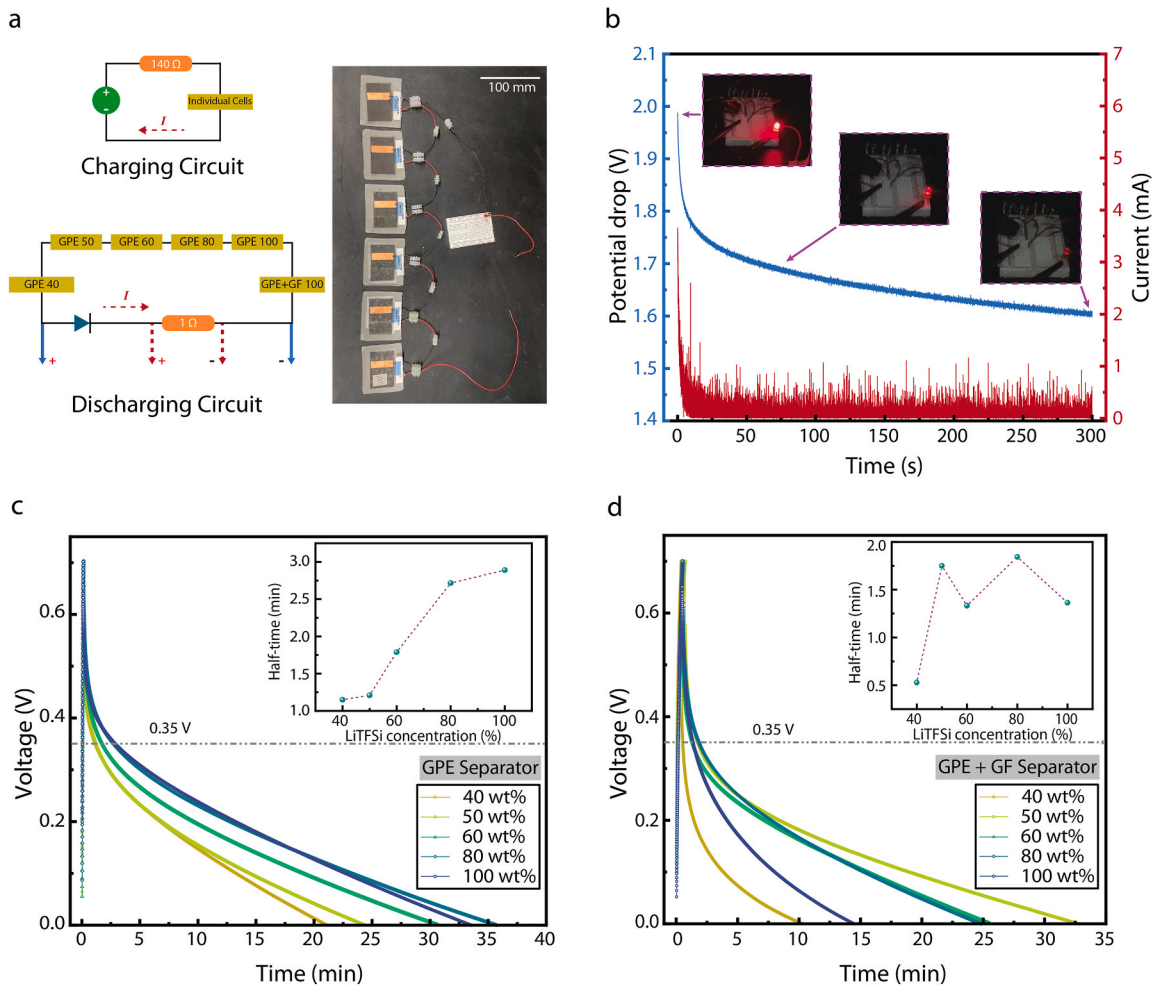

Fig. 5. Proof-of-concept demonstration of the prototype SSC cells. a) Image of the charging setup for each individual cell, and the discharge setup allowing to power a red light emitting diode (LED) for demonstration. In the discharging circuit, the connection point to measure the potential V across the 6 cells connected in series is shown in blue, and for the current *I* across the 1 Ω resistor in red. The adjacent image shows the connected cells before performing discharge through the LED. b) The recorded voltage and current during discharging of the 6 cells while powering the red LED. The insets show the different states of the LED along the discharge curve. The self-discharge phenomena are presented as the potential drop over time for: c) the cells with GPE separator, and d) the cells with GPE impregnated GF separator, where the corresponding insets show the time required for the voltage to decrease by half (0.35 V).

sheets led to a lower specific capacitance and a higher resistance, their improved mechanical stability and tuneable electrochemical properties with varying salt concentrations provided valuable insights into the electrochemical processes. The implementation of GF into the GPE separator improved the mechanical stiffness of the produced cell. All produced cells showed improved multifunctional properties indicating a balance between flexural properties and capacitance. Future research can optimize this interface to enhance both electrical and structural performance, making supercapacitors more practical for real-world usage. Finally, the proof-of-concept was achieved by powering a red LED with the fabricated structural supercapacitor cells. The reported findings pave the way for further refinement of multifunctional composites, which are crucial for developing robust, lightweight, and integrated energy storage systems suitable for applications in aerospace, automotive, robotic, and wearable technologies.

CRediT authorship contribution statement

Sian Ying Chen: Writing – review & editing, Writing – original draft, Investigation, Conceptualization. **Sourav Patranabish:** Writing – review & editing, Writing – original draft, Visualization, Validation, Formal analysis, Data curation. **Kathrin Weiland:** Writing – review & editing, Writing – original draft, Validation, Formal analysis. **Qixiang Jiang:** Writing – review & editing, Writing – original draft, Validation. **Alexander Bismarck:** Writing – review & editing, Writing – original draft, Validation. **Ludovic Jourdin:** Writing – review & editing, Validation. **Kunal Masania:** Writing – review & editing, Writing – original draft, Supervision, Conceptualization.

Declaration of competing interest

The authors declare that they have no known competing financial interests or personal relationships that could have appeared to influence the work reported in this paper.

Acknowledgments

We acknowledge fundings from the European Union (ERC Consolidator Grant, AM-IMATE, 101088968) and from the project "C1to6: CO_2 into hexanoic acid using microbial electrosynthesis" (NWO OTP 19771). The authors also dedicate this work to the memory of Hsiao Chih Chen, the father of Sian Ying Chen.

Appendix A. Supplementary data

Supplementary data to this article can be found online at https://doi.

org/10.1016/j.compscitech.2026.111585.

Data availability

Data will be made available on request.

References

[1] IEA, Global CO2 Emissions in Transport by Mode in the Sustainable Development Scenario, 2000-2070, IEA, Paris, 2020.
[2] E. Terrenoire, D. Hauglustaine, T. Gasser, O. Penanhoat, Environ. Res. Lett. 14 (2019) 084019.
[3] M.J. Nieuwenhuijsen, Environ. Int. 140 (2020) 105661.
[4] B. Nykvist, O. Olsson, Joule 5 (2021) 901–913.
[5] P.H. Camargos, P.H. dos Santos, I.R. dos Santos, G.S. Ribeiro, R.E. Caetano, Int. J. Energy Res. 46 (2022) 19258–19268.
[6] G.G. Njema, R.B.O. Ouma, J.K. Kibet, Journal of renewable energy 2024 (2024) 2329261.
[7] I. Staack, A. Sobron, P. Krus, CEAS Aeronautical Journal 12 (2021) 803–819.
[8] R. de Vries, R.E. Wolleswinkel, M. Hoogreef, R. Vos, in: Proceedings of the AIAA SCITECH 2024 Forum, 2024, p. 1490.
[9] L.E. Asp, K. Bouton, D. Carlstedt, S. Duan, R. Harnden, W. Johannisson, M. Johansen, M.K. Johansson, G. Lindbergh, F. Liu, Adv. Energy Sustain. Res. 2 (2021) 2000093.
[10] L.E. Asp, M. Johansson, G. Lindbergh, J. Xu, D. Zenkert, Funct. Compos. Struct. 1 (2019) 042001.
[11] E.S. Greenhalgh, S. Nguyen, M. Valkova, N. Shirshova, M.S. Shaffer, A. Kucernak, Compos. Sci. Technol. 235 (2023) 109968.
[12] B.K. Deka, A. Hazarika, J. Kim, Y.B. Park, H.W. Park, Int. J. Energy Res. 41 (2017) 1397–1411.
[13] K.-Y. Chan, B. Jia, H. Lin, N. Hameed, J.-H. Lee, K.-T. Lau, Composite Structures vol. 188, 2018, pp. 126–142.
[14] L.E. Asp, E.S. Greenhalgh, Composites Science and Technology vol 101, 2014, pp. 41–61.
[15] E.S. Greenhalgh, S. Nguyen, L.E. Asp, A. Bici, A. Bismarck, D. Fam, M. Johansson, G. Lindbergh, J.L. Lutkenhaus, M.S.P. Shaffer, N. Shirshova, M. Srinivasan, J. Xu, D. Zenkert, Adv. Energy Mater. (2025) e04702 n/a.
[16] E. Karadotcheva, S.N. Nguyen, E.S. Greenhalgh, M.S. Shaffer, A.R. Kucernak, P. Linde, Energies 14 (2021) 6006.
[17] S.N. Nguyen, A. Millereux, A. Pouyat, E.S. Greenhalgh, M.S. Shaffer, A. R. Kucernak, P. Linde, J. Aircraft 58 (2021) 677–687.
[18] A. Ishfaq, S.N. Nguyen, E.S. Greenhalgh, M.S. Shaffer, A.R. Kucernak, L.E. Asp, D. Zenkert, P. Linde, J. Compos. Mater. 57 (2023) 817–827.
[19] J. F. Snyder, D. J. O'Brien and E. D. Wetzel, in Handbook of Solid State Batteries, DOI: 10.1142/9789814651905_0019, pp. 657-699.
[20] M. Liu, J.C. Liu, Y. Zhang, X. Han, H. Li, Z.H. Huang, T. Ma, Chemelectrochem 12 (2025) e202400513.
[21] J. Anurangi, M. Herath, D.T. Galhena, J. Epaarachchi, Adv. Compos. Mater. 32 (2023) 942–986.
[22] S.M. Shalouf, J. Zhang, C.H. Wang, Plast, Rubber Compos. 43 (2014) 98–104.
[23] Y. Wang, X. Qiao, C. Zhang, X. Zhou, J. Energy Storage 26 (2019) 100968.
[24] K. Wang, Z. Wang, C. Wang, X. Zhang, L. Wu, J. Energy Storage 98 (2024) 113129.
[25] H. Qian, H. Diao, N. Shirshova, E.S. Greenhalgh, J.G. Steinke, M.S. Shaffer, A. Bismarck, J. Colloid Interface Sci. 395 (2013) 241–248.
[26] P. Sagar, I.R. Hamdani, T. Levato, V. Giannini, G. Das, Mater. Adv. (2025).
[27] X.F. Sánchez-Romate, A.D. Bosque, J. Artigas-Arnaudas, B.K. Muñoz, M. Sánchez, A. Ureña, Electrochim. Acta 370 (2021) 137746.
[28] N. Shirshova, H. Qian, M.S.P. Shaffer, J.H.G. Steinke, E.S. Greenhalgh, P.T. Curtis, A. Kucernak, A. Bismarck, Compos. Appl. Sci. Manuf. 46 (2013) 96–107.
[29] V. Kumaravel, J. Bartlett, S.C. Pillai, Adv. Energy Mater. 11 (2021) 2002869.
[30] A. Javaid, K. Ho, A. Bismarck, J. Steinke, M. Shaffer, E. Greenhalgh, J. Compos. Mater. 50 (2016) 2155–2163.
[31] Q. Wendong, J. Dent, V. Arrighi, L. Cavalcanti, M.S.P. Shaffer, N. Shirshova, Multifunctional Materials 4 (2021) 035003.
[32] T. Harte, B. Dharmasiri, P. Coia, D.J. Eyckens, L.C. Henderson, J. Mol. Liq. 402 (2024) 124689.
[33] S. Alipoori, S. Mazinani, S.H. Aboutalebi, F. Sharif, J. Energy Storage 27 (2020) 101072.
[34] L. Elbinger, M. Enke, N. Ziegenbalg, J.C. Brendel, U.S. Schubert, Energy Storage Mater. 65 (2024) 103063.
[35] E. Senokos, Y. Ou, J.J. Torres, F. Sket, C. González, R. Marcilla, J.J. Vilatela, Sci. Rep. 8 (2018) 3407.
[36] A. Javaid, Imperial College London, 2012.
[37] Y. Wu, Y. Li, Y. Wang, Q. Liu, Q. Chen, M. Chen, J. Energy Chem. 64 (2022) 62–84.
[38] Y. Xu, S. Pei, Y. Yan, L. Wang, G. Xu, S. Yarlagadda, T.-W. Chou, ACS Appl. Mater. Interfaces 13 (2021) 11774–11782.
[39] Y. Xu, W. Lu, G. Xu, T.-W. Chou, Compos. Sci. Technol. 204 (2021) 108636.
[40] H.D. Asfaw, A. Kucernak, E.S. Greenhalgh, M.S. Shaffer, Compos. Sci. Technol. 238 (2023) 110042.
[41] A. Javaid, M. Irfan, Mater. Res. Express 6 (2018) 016310.
[42] J. Artigas-Arnaudas, B.K. Muñoz, M. Sánchez, J. de Prado, M.V. Utrilla, A. Ureña, Appl. Compos. Mater. (2022) 1–12.
[43] B.K. Deka, A. Hazarika, O. Kwon, D. Kim, Y.-B. Park, H.W. Park, Chem. Eng. J. 325 (2017) 672–680.
[44] E. Senokos, D.B. Anthony, N. Rubio, M.C. Ribadeneyra, E.S. Greenhalgh, M. S. Shaffer, Adv. Funct. Mater. 33 (2023) 2212697.
[45] O. Hubert, N. Todorovic, A. Bismarck, Compos. Sci. Technol. 217 (2022) 109126.
[46] H. Qian, H.L. Diao, M. Houllé, J. Amadou, N. Shirshova, E. Greenhalgh, M.S.P. Shaffer, A. Bismarck, Carbon fibre modifications for composite structural power devices, ECCM15 - 15TH EUROPEAN CONFERENCE ON COMPOSITE MATERIALS, Venice, Italy, 24-28 June 2012.
[47] Y. Ding, G. Qi, Q. Cui, J. Yang, B. Zhang, S. Du, Energy Fuel. 36 (2022) 2171–2178.
[48] N.A. Elessawy, J. El Nady, W. Wazeer, A.B. Kashyout, Sci. Rep. 9 (2019) 1129.
[49] B. Fales, N. Fujamade, J. Oomens, M. Rodgers, J. Am. Soc. Mass Spectrom. 22 (2011).
[50] Z. He, Q. Cao, B. Jing, X. Wang, Y. Deng, RSC Adv. 7 (2017) 3240–3248.
[51] S. Abbrent, J. Plestil, D. Hlavata, J. Lindgren, J. Tegenfeldt, Å. Wendsjö, Polymer 42 (2001) 1407–1416.
[52] Q. Li, Y. Xu, S. Zheng, X. Guo, H. Xue, H. Pang, Small 14 (2018) 1800426.
[53] J. Zhang, Y. Li, Z. Chen, Q. Liu, Q. Chen, M. Chen, Energy Environ. Mater. 6 (2023) e12573.
[54] G.-Q. Han, Y.-R. Liu, W.-H. Hu, B. Dong, X. Li, X. Shang, Y.-M. Chai, Y.-Q. Liu, C.-G. Liu, J. Electrochem. Soc. 163 (2015) H67.
[55] P. Jin, X. Zhang, M. Zhen, J. Wang, RSC Adv. 6 (2016) 10938–10942.
[56] Y. He, W. Chen, X. Li, Z. Zhang, J. Fu, C. Zhao, E. Xie, ACS Nano 7 (2013) 174–182.
[57] B. Vidhyadharan, I.I. Misnon, R. Abd Aziz, K. Padmasree, M.M. Yusoff, R. Jose, J. Mater. Chem. A 2 (2014) 6578–6588.
[58] Y. Huang, Y. Li, Z. Hu, G. Wei, J. Guo, J. Liu, J. Mater. Chem. A 1 (2013) 9809–9813.
[59] K. Krishnamoorthy, G.K. Veerasubramani, P. Pazhamalai, S.J. Kim, Electrochim. Acta 190 (2016) 305–312.
[60] A.C. Lazanas, M.I. Prodromidis, ACS Meas. Sci. Au 3 (2023) 162–193.
[61] I. Yang, S.-G. Kim, S.H. Kwon, M.-S. Kim, J.C. Jung, Electrochim. Acta 223 (2017) 21–30.
[62] C. Lei, F. Markoulidis, Z. Ashitaka, C. Lekakou, Electrochim. Acta 92 (2013) 183–187.
[63] E. Casero, A. Parra-Alfambra, M. Petit-Domínguez, F. Pariente, E. Lorenzo, C. Alonso, Electrochem. Commun. 20 (2012) 63–66.
[64] B.-A. Mei, J. Lau, T. Lin, S.H. Tolbert, B.S. Dunn, L. Pilon, J. Phys. Chem. C 122 (2018) 24499–24511.
[65] B.-A. Mei, O. Munteshari, J. Lau, B. Dunn, L. Pilon, J. Phys. Chem. C 122 (2018) 194–206.
[66] Q. Kang, Z. Zhuang, Y. Liu, Z. Liu, Y. Li, B. Sun, F. Pei, H. Zhu, H. Li, P. Li, Adv. Mater. 35 (2023) 2303460.
[67] A.R. Finney, I.J. McPherson, P.R. Unwin, M. Salvalaglio, Chem. Sci. 12 (2021) 11166–11180.
[68] M.Z. Bazant, B.D. Storey, A.A. Kornyshev, Phys. Rev. Lett. 106 (2011) 046102.
[69] J.P. de Souza, Z.A. Goodwin, M. McEldrew, A.A. Kornyshev, M.Z. Bazant, Phys. Rev. Lett. 125 (2020) 116001.
[70] X. Huan, B. Hu, Z. Ji, C. Gao, F. Zhou, J. Yu, B. Du, Y. Zhao, Compos. Commun. 56 (2025) 102391.
[71] N.S. Hudak, A.D. Schlichting, K. Eisenbeiser, J. Electrochem. Soc. 164 (2017) A691.
[72] R. Reece, C. Lekakou, P.A. Smith, Mater. Sci. Technol. 35 (2019) 368–375.
[73] G. Qi, S. Nguyen, D.B. Anthony, A.R. Kucernak, M.S. Shaffer, E.S. Greenhalgh, Multifunctional Materials 4 (2021) 034001.
[74] M. Shi, W. Yang, Z. Zhang, M. Zhao, Z.L. Wang, X. Lu, J. Mater. Chem. A 10 (2022) 2966–2972.
[75] H. Huang, H. Wu, Y. Xu, F. Xu, Int. J. Biol. Macromol. 276 (2024) 133896.
[76] E.S. Greenhalgh, J. Ankersen, L.E. Asp, A. Bismarck, Q. Fontana, M. Houlle, G. Kalinka, A. Kucernak, M. Mistry, S. Nguyen, J. Compos. Mater. 49 (2015) 1823–1834.
[77] H. Qian, A.R. Kucernak, E.S. Greenhalgh, A. Bismarck, M.S.P. Shaffer, ACS Appl. Mater. Interfaces 5 (2013) 6113–6122.
[78] A. Javaid, O. Khalid, A. Shakeel, S. Noreen, J. Energy Storage 33 (2021) 102168.